

Article

A Simple-FSDT-Based Isogeometric Method for Piezoelectric Functionally Graded Plates

Tao Liu ^{1,2}, Chaodong Li ¹, Chao Wang ^{2,*}, Joel Weijia Lai ³ and Kang Hao Cheong ^{3,4,*}

¹ Department of Mechatronic Engineering and Automation, Shanghai University, Shanghai 200072, China; lt_ahut@126.com (T.L.); cdli@staff.shu.edu.cn (C.L.)

² Department of Mechanical Engineering, Anhui University of Technology, Ma'anshan 243002, China

³ Science, Mathematics and Technology Cluster, Singapore University of Technology and Design (SUTD), 8 Somapah Road, Singapore 487372, Singapore; joel_lai@mymail.sutd.edu.sg

⁴ SUTD-Massachusetts Institute of Technology International Design Centre, Singapore 487372, Singapore

* Correspondence: cw2013@ahut.edu.cn (C.W.); kanghao_cheong@sutd.edu.sg (K.H.C.)

Received: 16 November 2020; Accepted: 4 December 2020; Published: 6 December 2020

Abstract: An efficient isogeometric analysis method (IGA) based on a simple first-order shear deformation theory is presented to study free vibration, static bending response, dynamic response, and active control of functionally graded plates (FGPs) integrated with piezoelectric layers. Based on the neutral surface, isogeometric finite element motion equations of piezoelectric functionally graded plates (PFGPs) are derived using the linear piezoelectric constitutive equation and Hamilton's principle. The convergence and accuracy of the method for PFGPs with various mechanical and electrical boundary conditions have been investigated via free vibration analysis. In the dynamic analysis, both time-varying mechanical and electrical loads are involved. A closed-loop control method, including displacement feedback control and velocity feedback control, is applied to the static bending control and the dynamic vibration control analysis. The numerical results obtained are accurate and reliable through comparisons with various numerical and analytical examples.

Keywords: isogeometric analysis method; simple first-order shear deformation theory; piezoelectric functionally graded plates; neutral surface; dynamic response; closed loop control

1. Introduction

Functionally graded materials (FGMs) [1] have been used extensively in the aerospace, nuclear power industries, biomedical field, and other applications [2–4] for their superior thermo-mechanical properties, such as low thermal conductivity and high thermal resistance. Classified as smart materials, piezoelectric materials are also known for their piezoelectric effects [5] (used as sensors) and converse piezoelectric effects (used as actuators). Unique electro-mechanical coupling characteristics of piezoelectric materials enable them to be applied in the fields of health monitoring and structural control. Accordingly, by fabricating (or embedding) piezoelectric materials on the surface (inside) of functionally graded beams, plates, shells, and other structures, they can respond rapidly according to their physical characteristics and shape changes, when the external environment changes.

Piezoelectric functionally graded plates (PFGPs) are one of the basic structural forms of piezoelectric functionally graded structures. Traditional numerical methods of PFGPs consume a mass of computational meshes based on the conventional three-dimensional elastic theory framework. To overcome these shortcomings, scholars combined various numerical methods with equivalent single layer theory [6] for predicting the behaviors of PFGPs [7,8]. The finite element method (FEM) has always been one of the popular methods to study PFGPs. Ray et al. [9] and Loja

et al. [10] presented investigation for the static response analysis of PFGPs. He et al. [11] employed the piezoelectric materials to investigate the dynamic vibration control of functionally graded plates (FGPs) by using the classical plate theory (CPT). Similarly, Liew et al. [12,13] studied the active control of FGPs with distributed piezoelectric materials under thermal loads based on the first-order shear deformation theory (FSDT). Aryana et al. [14] proposed a method to identify the most sensitive design variables that affect the dynamic characteristics of the structure. Using a cell-based smoothed discrete shear gap method, Nguyen-Quang et al. [15] studied the static and dynamic control analysis of FGPs bonded with piezoelectric actuators and sensors. In this method, each parent triangle element is divided into three sub-triangle elements, and the discrete shear gap method is used in each sub-triangle element to eliminate the shear-locking effects [16]. Then, the strain smoothing technology is applied in the whole parent triangle element to solve the defect of rigidity of triangle elements in FEM. By using the higher-order shear deformation theory (HSDT), Fakhari et al. [17,18] analyzed the nonlinear free and forced vibration, as well as nonlinear vibration control of PFGPs in thermal environments. Recently, a generalized C^0 -type HSDT polygonal finite element method was presented by Nguyen et al. [19] for investigating the active control of smart, functionally graded metal foam plates reinforced by graphene platelets. To avoid the decrease in the calculation accuracy [20,21] caused by element distortion in the FEM, various scholars also attempted to use the mesh-free method to analyze the behaviors of PFGPs. Using the element-free Galerkin method, Dai et al. [22] investigated the static, active control analysis of FGPs with surface-bonded piezoelectric materials in thermal environments. The stability of PFGPs subjected to distributed thermo-electro-mechanical loads was studied by Chen et al. [23]. The radial point interpolation method was implemented to investigate the geometrically nonlinear response of PFGPs under mechanical and electrical loads by Hossein et al. [24]. Considering the stability of the plate in vibration control, Selim et al. [25] studied the active control of two types of PFGP structures. They pointed out that for the structure of two piezoelectric layers distributed symmetrically on the upper and lower surfaces of the FGPs, due to the stretching–bending coupling effect, the velocity feedback control in the active vibration control is unstable when the gradient index is in the range of $0 < n < \infty$.

Although the FEM and mesh-free methods have achieved considerable success in the analysis of piezoelectric smart structures, there continues to be strong interest in new numerical methods. Recently, an isogeometric analysis (IGA) method was proposed by Hughes et al. [26]. Because of the advantages of high-order continuity and simple meshing, Phung-Van et al. [27] employed IGA to study the nonlinear dynamic response analysis of PFGPs under thermo-electro-mechanical loads. Similar studies of smart piezoelectric composite plates were developed by the same authors in the literature [28,29]. Along the same line, Nguyen et al. [30] and Nguyen-Quang et al. [31] presented developments of isogeometric analysis of piezoelectric, functionally graded porous plates reinforced by graphene platelets, and laminated carbon nanotube-reinforced composite plates bonded with piezoelectric materials, respectively.

The above studies on the dynamic analysis of piezoelectric smart structures are focused on the dynamic response of structures under mechanical loads. Few people pay attention to the dynamic response of the structures under time-varying voltage loads. However, many piezoelectric smart structures, such as piezoelectric motors [32] and robots [33], realize their motions precisely by utilizing the dynamic response under voltage loads. In addition, for the PFGPs, the presence of additional electric potential fields will result in more complicated mathematical modelling. Hence, a low-cost, efficient numerical method without loss of accuracy is extremely important. Most current approaches used CPT, FSDT, and HSDTs for the analysis of PFGPs. In these plate theories, CPT has the least amount of calculation because it has only three unknowns, but it is only valid for the thin plates due to the shear deformation effects being ignored [34]. The computational cost of FSDTs and HSDTs is more expensive than CPT because they have five or more unknowns. It is worth noting that Thai et al. [35,36] proposed a new simple first-order shear deformation theory (S-FSDT) with only four unknowns. Compared with FSDTs and HSDTs, the decrease of unknowns makes S-FSDT have a certain advantage in computational efficiency. Moreover, because S-FSDT is derived from FSDT, it is suitable for both thin

and thick plates. The accuracy and validity of this theory for analyzing the static bending, buckling, free vibration [37], and geometrically nonlinear responses [38] of FGP's have been demonstrated.

In summary, the main motivations of this paper are: (i) there are no studies on isogeometric analysis for the analysis of PFGPs based on the simple first-order shear deformation theory, and the present study can fill this research gap; (ii) the S-FSDT-based IGA method has only four unknowns, and it is easily applied to the open-source IGA frameworks; (iii) the investigation of dynamic response of the structures under time-varying voltage loads can provide a more comprehensive understanding of the mechanical behavior of piezoelectric smart structures.

Therefore, in this paper, we propose an approach based on S-FSDT and the NURBS-based isogeometric analysis for analyzing the mechanical behavior of the PFGPs. The mechanical displacement field and electric potential field in PFGPs are approximated using the NURBS basis functions. Isogeometric finite element equations of PFGPs are derived through the linear piezoelectric constitutive equation and Hamilton's variational principle. The dynamic response of PFGPs under mechanical loads and voltage loads are studied by using the Newmark- β direct integration method. Additionally, the static and dynamic closed-loop control are used for controlling the shapes and vibration of the plates.

2. Mathematical Model

The piezoelectric functionally graded plate is shown in Figure 1 with the size of $a \times b \times h_t$ (length \times width \times thicknesses), in which $h_t = h_f + 2h_p$, where h_f and h_p are the thicknesses of the FGM layer and each piezoelectric layer. The polarization directions of the upper and lower piezoelectric layers are downward and upward, respectively.

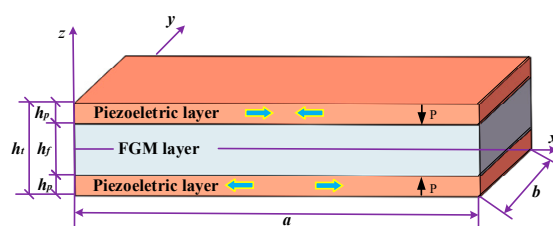


Figure 1. Structure diagram of the PFGP.

2.1. Functionally Graded Materials

The material properties of functionally graded plates along the thickness direction can be described as

$$P(z) = (P_m - P_c)V_m(z) + P_c \tag{1}$$

The volume fraction of metal materials is defined as

$$V_m(z) = \left(\frac{1}{2} + \frac{z}{h_f}\right)^n, \tag{2}$$

where the subscript symbols m and c represent the metal and ceramic, respectively; P_c and P_m are the corresponding material properties, such as mass density (ρ), Young's modulus (E), and various other properties; n is the gradient index. Figure 2 shows the variation of the composition of the FGP with n . It is seen that as n increases, the less metal components in the plate.

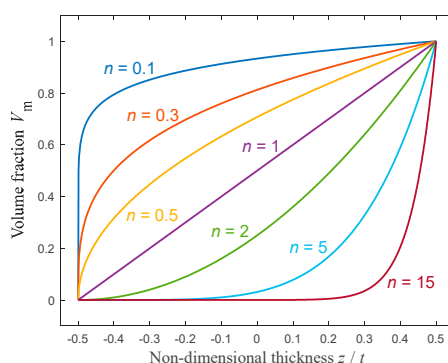


Figure 2. The volume fraction of the metal V_m varies with different n .

2.2. Mechanical Displacement and Strain Based on S-FSDT

For the simple first-order shear deformation theory, the unknowns are reduced from five to four using two assumptions [36]: first, the transverse displacement $w_0(x, y)$ in the standard FSDT is split into bending and shear parts, that is, $w_0 = w_b + w_s$; second, the rotations β_x and β_y are expressed using the partial derivatives of the transverse bending components, that is, $\beta_x = -\partial w_b / \partial x$ and $\beta_y = -\partial w_b / \partial y$.

The neutral surface is introduced to avoid the stretching–bending coupling effect. Hence, the displacement formulation of the S-FSDT can be written as

$$u(x, y, z) = \bar{u}(x, y) + (z - z_0) \hat{u}(x, y), \tag{3}$$

where $u = \{u \ v \ w\}^T$, $\bar{u} = \{u_0 \ v_0 \ w_b + w_s\}^T$, and $\hat{u} = \{-\partial w_b / \partial x \ \partial w_b / \partial y \ 0\}^T$. In which, u_0 and v_0 represent the displacements of the neutral plane of the plate in x and y directions, respectively; β_x and β_y are the rotation variables; z_0 is the distance between the mid and neutral surface, which can be denoted as

$$z_0 = \frac{\int_{-h_i/2}^{h_i/2} zE(z)dz}{\int_{-h_i/2}^{h_i/2} E(z)dz}. \tag{4}$$

The geometric strains $\tilde{\epsilon}$ can be given as

$$\tilde{\epsilon} = \begin{Bmatrix} \epsilon \\ \gamma \end{Bmatrix}, \tag{5}$$

where

$$\epsilon = \{ \epsilon_x \ \epsilon_y \ \gamma_{xy} \}^T = \epsilon_0 - (z - z_0) \kappa, \tag{6a}$$

$$\gamma = \{ \gamma_{xz} \ \gamma_{yz} \}^T = \left\{ \frac{\partial w_s}{\partial x} \ \frac{\partial w_s}{\partial y} \right\}^T, \tag{6b}$$

with

$$\epsilon_0 = \{ u_{0,x} \ v_{0,y} \ u_{0,y} + v_{0,x} \}^T, \tag{7a}$$

$$\kappa = \{ \partial^2 w_b / \partial x^2 \ \partial^2 w_b / \partial y^2 \ 2\partial^2 w_b / \partial x \partial y \}^T. \tag{7b}$$

2.3. Constitutive Relationship

For the functionally graded plates, the constitutive relationship between the geometric stresses and strains can be denoted as

$$\sigma_f = Q_f \tilde{\epsilon}, \tag{8}$$

where

$$Q_f = \begin{bmatrix} Q & 0 \\ 0 & G \end{bmatrix}, \tag{9}$$

with

$$Q = \begin{bmatrix} Q_{11} & Q_{12} & 0 \\ Q_{21} & Q_{22} & 0 \\ 0 & 0 & Q_{66} \end{bmatrix}, \quad G = \begin{bmatrix} Q_{44} & 0 \\ 0 & Q_{55} \end{bmatrix}, \tag{10}$$

in which

$$Q_{11} = Q_{22} = \frac{E(z)}{1 - \nu(z)^2}, \quad Q_{12} = Q_{21} = \frac{\nu(z)E(z)}{1 - \nu(z)^2}, \quad Q_{44} = Q_{55} = \frac{E(z)}{2(1 + \nu(z))}. \tag{11}$$

For the piezoelectric layers, the linear piezoelectric constitutive equation [18] is given by:

$$\begin{bmatrix} \sigma_p \\ \mathbf{D} \end{bmatrix} = \begin{bmatrix} Q_p & -\mathbf{e}^T \\ \mathbf{e} & \mathbf{g} \end{bmatrix} \begin{bmatrix} \tilde{\epsilon} \\ \mathbf{E} \end{bmatrix}, \tag{12}$$

where σ_p is the stress; \mathbf{D} is the electrical displacement; \mathbf{g} is the permittivity constant matrix; and \mathbf{e} is the piezoelectric stress constant matrix. Q_p is the elastic constant of piezoelectric materials with the similar form of Q_f .

Only the electric field component in the z direction is considered. Hence, the electric field \mathbf{E} is calculated by

$$\mathbf{E} = -\text{grad}\varphi = \{0 \quad 0 \quad E_z\}^T. \tag{13}$$

The stress resultants in the PFGPs are expressed as

$$\begin{Bmatrix} \mathbf{N} \\ \mathbf{M} \\ \mathbf{P} \end{Bmatrix} = \hat{\mathbf{c}} \begin{Bmatrix} \epsilon_0 \\ \boldsymbol{\kappa} \\ \boldsymbol{\gamma} \end{Bmatrix} - \begin{Bmatrix} \mathbf{N}^p \\ \mathbf{M}^p \\ \mathbf{0} \end{Bmatrix}, \tag{14}$$

where

$$\hat{\mathbf{c}} = \begin{bmatrix} \mathbf{D}_{mb} & \mathbf{0} \\ \mathbf{0} & \mathbf{C}_s \end{bmatrix}, \tag{15}$$

with

$$\mathbf{D}_{mb} = \begin{bmatrix} \mathbf{A} & \mathbf{B} \\ \mathbf{B} & \mathbf{D} \end{bmatrix}, \quad \mathbf{C}_s = k \int_{-h_i/2}^{h_i/2} G_{ij} dz, \quad i, j = 4, 5, \tag{16}$$

where k is the shear correction factor and it is set to be 5/6, and

$$A_{ij} = \int_{-h_i/2}^{h_i/2} Q_{ij} dz, \quad i, j = 1, 2, 6, \tag{17a}$$

$$D_{ij} = \int_{-h_i/2}^{h_i/2} (z - z_0)^2 Q_{ij} dz, \quad i, j = 1, 2, 6, \tag{17b}$$

since the introduction of neutral surface [39], $B_{ij} = 0$.

The forces and bending moments generated by the electric field can be calculated by

$$\mathbf{N}^p = \begin{Bmatrix} N_x^p \\ N_y^p \\ N_{xy}^p \end{Bmatrix} = \int_{\frac{h_f}{2}}^{\frac{h_f}{2}+h_p} \mathbf{e}^T \mathbf{E} dz + \int_{\frac{h_f}{2}-h_p}^{\frac{h_f}{2}} \mathbf{e}^T \mathbf{E} dz \tag{18}$$

$$\mathbf{M}^p = \begin{Bmatrix} M_x^p \\ M_y^p \\ M_{xy}^p \end{Bmatrix} = \int_{\frac{h_f}{2}}^{\frac{h_f}{2}+h_p} \mathbf{e}^T \mathbf{E} (z - z_0) dz + \int_{\frac{h_f}{2}-h_p}^{\frac{h_f}{2}} \mathbf{e}^T \mathbf{E} (z - z_0) dz \tag{19}$$

2.4. Nurbs-Based Isogeometric Analysis

In this section, the displacements and electric potential are approximated by using the NURBS basis functions. Then, the isogeometric finite element motion equations are derived through the variational form of the PFGPs' motion equations.

2.4.1. Basis Functions

Combining an additional individual weight $\vartheta_{i,j}$ with the tensor product of B-spline basis functions in two parametric dimensions ξ and η with two knot vectors $\Psi(\xi) = \{\xi_1 = 0, \dots, \xi_i, \dots, \xi_{m+p+1} = 1\}$ and $\Psi(\eta) = \{\eta_1 = 0, \dots, \eta_j, \dots, \eta_{n+q+1} = 1\}$, the two-dimensional (2D) NURBS basis function can be written as [40]

$$R_{i,j}^{p,q}(\xi, \eta) = \frac{G_{i,p}(\xi)H_{j,q}(\eta)J_{i,j}}{\sum_{i=1}^m \sum_{j=1}^n G_{i,p}(\xi)H_{j,q}(\eta)J_{i,j}} \tag{20}$$

where G and H are B-spline basis functions, respectively; p and q are the orders.

2.4.2. Approximation of Mechanical Displacement

The mechanical displacement can be approximated as

$$\mathbf{u}(\xi, \eta) = [u_0 \quad v_0 \quad w_b \quad w_s]^T = \sum_{k=1}^{m \times n} R_k(\xi, \eta) \mathbf{d}_k \tag{21}$$

where $\mathbf{d}_k = [u_{0k} \quad v_{0k} \quad w_{bk} \quad w_{sk}]^T$ is the unknown displacement vector of control point k and $R_k(\xi, \eta)$ is the basis function defined in (20).

The strain functions can be achieved by substituting (21) into (6) and (7), which yields

$$\boldsymbol{\varepsilon}_0 = \sum_{k=1}^{m \times n} [\mathbf{B}_k^m]^T \mathbf{d}_k \quad \boldsymbol{\kappa} = \sum_{k=1}^{m \times n} [\mathbf{B}_k^b]^T \mathbf{d}_k \quad \boldsymbol{\gamma} = \sum_{k=1}^{m \times n} [\mathbf{B}_k^s]^T \mathbf{d}_k \tag{22}$$

where

$$\mathbf{B}_k^m = \begin{bmatrix} R_{k,x} & 0 & 0 & 0 \\ 0 & R_{k,y} & 0 & 0 \\ R_{k,y} & R_{k,x} & 0 & 0 \end{bmatrix} \tag{23a}$$

$$\mathbf{B}_k^b = \begin{bmatrix} 0 & 0 & R_{k,xx} & 0 \\ 0 & 0 & R_{k,yy} & 0 \\ 0 & 0 & 2R_{k,xy} & 0 \end{bmatrix} \tag{23b}$$

$$\mathbf{B}_k^s = \begin{bmatrix} 0 & 0 & 0 & R_{k,x} \\ 0 & 0 & 0 & R_{k,y} \end{bmatrix} \tag{23c}$$

2.4.3. Approximation of the Electric Potential Field

The electric potential is assumed to vary linearly along the thickness [41], expressed as

$$\varphi = \mathbf{R}_k \boldsymbol{\varphi}_k, \tag{24}$$

where $\boldsymbol{\varphi}_k$ is the generalized nodal electric potential vector.

Substituting (24) into (13) yields

$$\mathbf{E} = -\mathbf{B}_\varphi \boldsymbol{\varphi}_k, \tag{25}$$

with

$$\mathbf{B}_\varphi = \{0 \quad 0 \quad R_k/h_p\}^T. \tag{26}$$

2.4.4. Isogeometric Finite Element Motion Equations

The variational form of the equations of motion for the plate can be obtained by Hamilton's principle

$$\delta \int_{t_1}^{t_2} L dt = \delta \int_{t_1}^{t_2} (T - U + W_{ext}) dt = 0, \tag{27}$$

where L is the total energy, including kinetic energy T , potential energy U , and external work W_{ext} , with

$$T = \int_V \frac{1}{2} \mathbf{m} \dot{\mathbf{u}}^T \dot{\mathbf{u}} dV, \tag{28a}$$

$$U = \int_V \left(\frac{1}{2} \tilde{\boldsymbol{\varepsilon}}^T \mathbf{Q} \tilde{\boldsymbol{\varepsilon}} - \tilde{\boldsymbol{\varepsilon}}^T \mathbf{e}^T \mathbf{E} - \frac{1}{2} \mathbf{E}^T \mathbf{g} \mathbf{E} \right) dV, \tag{28b}$$

$$W_{ext} = \int_\Omega (\mathbf{u}^T \mathbf{f}_s - \boldsymbol{\varphi} \mathbf{q}_s) d\Omega, \tag{28c}$$

where \mathbf{u} is the displacement; $\dot{\mathbf{u}}$ is velocity; \mathbf{q}_s denotes the surface charge; \mathbf{f}_s is the surface loads.

By substituting (8), (12), (22), (23), and (25) into (27), the governing equations of PFGPs can be denoted as

$$\mathbf{M}_{uu} \ddot{\mathbf{d}} + \mathbf{K}_{uu} \mathbf{d} + \mathbf{K}_{u\varphi} \boldsymbol{\varphi} = \mathbf{f}, \tag{29a}$$

$$\mathbf{K}_{\varphi u} \mathbf{d} - \mathbf{K}_{\varphi\varphi} \boldsymbol{\varphi} = \mathbf{f}_\varphi, \tag{29b}$$

where

$$\mathbf{K}_{uu} = \int_V \mathbf{B}_u^T \tilde{\mathbf{c}} \mathbf{B}_u dV, \mathbf{K}_{u\varphi} = \int_V \mathbf{B}_u^T \tilde{\mathbf{e}}^T \mathbf{B}_\varphi dV, \tag{30a}$$

$$\mathbf{K}_{\varphi\varphi} = \int_V \mathbf{B}_\varphi^T \mathbf{g} \mathbf{B}_\varphi dV, \mathbf{K}_{\varphi u} = \mathbf{K}_{u\varphi}^T, \mathbf{M}_{uu} = \int_V \boldsymbol{\Lambda}^T \mathbf{m} \boldsymbol{\Lambda} dV, \tag{30b}$$

$$\mathbf{f} = \int_\Omega f_z \bar{\boldsymbol{\Lambda}} d\Omega, \bar{\boldsymbol{\Lambda}} = [0 \quad 0 \quad R_k \quad R_k]^T, \tag{31a}$$

$$\mathbf{f}_\varphi = \int_\Omega R_k^T q_E d\Omega, \tag{31b}$$

and

$$\mathbf{B}_u = [(\mathbf{B}_k^m)^T \quad (\mathbf{B}_k^b)^T \quad (\mathbf{B}_k^s)^T]^T, \tag{32a}$$

$$\tilde{\mathbf{e}} = [\mathbf{e}_m^T \quad -(z - z_0) \mathbf{e}_m^T \quad \mathbf{e}_s^T], \tag{32b}$$

$$\mathbf{g} = \begin{bmatrix} k_{11} & 0 & 0 \\ 0 & k_{22} & 0 \\ 0 & 0 & k_{33} \end{bmatrix}, \tag{32c}$$

$$\mathbf{m} = \begin{bmatrix} I_0 & I_1 \\ I_1 & I_2 \end{bmatrix}, \tag{32d}$$

$$\mathbf{\Lambda} = [\mathbf{\Lambda}_1 \quad \mathbf{\Lambda}_2]^T, \tag{32e}$$

in which

$$\mathbf{e}_m = \begin{bmatrix} 0 & 0 & 0 \\ 0 & 0 & 0 \\ e_{31} & e_{32} & 0 \end{bmatrix}, \quad \mathbf{e}_s = \begin{bmatrix} 0 & e_{15} \\ e_{15} & 0 \\ 0 & 0 \end{bmatrix}, \tag{33a}$$

$$(I_0, I_1, I_2) = \int_{-ht/2}^{ht/2} \rho(z)(1, (z-z_0), (z-z_0)^2) dz, \tag{33b}$$

$$\mathbf{\Lambda}_1 = \begin{bmatrix} R_k & 0 & 0 & 0 \\ 0 & R_k & 0 & 0 \\ 0 & 0 & R_k & R_k \end{bmatrix}, \tag{33c}$$

$$\mathbf{\Lambda}_2 = \begin{bmatrix} 0 & 0 & R_{k,x} & 0 \\ 0 & 0 & R_{k,y} & 0 \\ 0 & 0 & 0 & 0 \end{bmatrix}. \tag{33d}$$

In (31), f_z is the transverse mechanical surface load; q_E is the charge density on the surface of piezoelectric layers.

$$q_E = k_{33} \frac{\bar{U}}{h_p}, \tag{34}$$

where \bar{U} is the electric potential applied on piezoelectric layers.

Eliminating the potential φ , (29) is rewritten as

$$\mathbf{M}_{uu} \ddot{\mathbf{d}} + \mathbf{K} \mathbf{d} = \mathbf{F}, \tag{35}$$

in which

$$\mathbf{K} = \mathbf{K}_{uu} + \mathbf{K}_{u\varphi} \mathbf{K}_{\varphi\varphi}^{-1} \mathbf{K}_{\varphi u}, \tag{36a}$$

$$\mathbf{F} = \mathbf{f} + \mathbf{K}_{u\varphi} \mathbf{K}_{\varphi\varphi}^{-1} \mathbf{f}_{\varphi}. \tag{36b}$$

Introducing Rayleigh damping, (35) is rewritten as

$$\mathbf{M}_{uu} \ddot{\mathbf{d}} + \mathbf{C}_R \dot{\mathbf{d}} + \mathbf{K} \mathbf{d} = \mathbf{F}, \tag{37}$$

where

$$\mathbf{C}_R = \alpha_R \mathbf{M}_{uu} + \beta_R \mathbf{K}_{uu}, \tag{38}$$

in which α_R and β_R are Rayleigh damping factors that can be confirmed through [42].

3. Closed-Loop Control

In this section, the static and dynamic closed-loop control of the FGPs by using piezoelectric sensors and actuators are studied. As shown in Figure 3, the upper piezoelectric layer serves as an actuator, and the lower piezoelectric layer serves as a sensor. The sensor generates electric charges because of the piezoelectric effect when the structure deforms. Then, these electric charges are

amplified as the input voltage of the actuator. On account of the converse piezoelectric effect, the actuator exerts a force opposite to the external mechanical loads to suppress the static bending or dynamic vibration of the structure, achieving the purpose of active control.

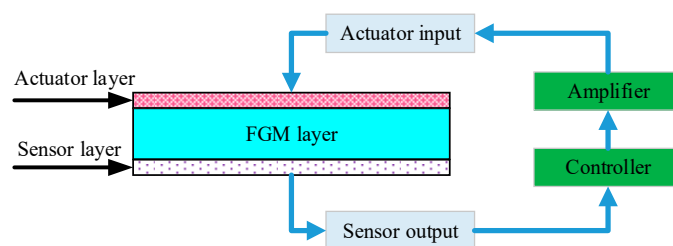


Figure 3. Diagram of the active control of the functionally graded plate (FGP) with surface-bonded a piezoelectric actuator and sensor.

According to the prior analysis, (29b) can be rewritten as

$$\mathbf{K}_{\varphi ua} \mathbf{d} - \mathbf{K}_{\varphi\varphi a} \boldsymbol{\phi}_a = \mathbf{f}_{\varphi a}, \tag{39}$$

$$\mathbf{K}_{\varphi us} \mathbf{d} - \mathbf{K}_{\varphi\varphi s} \boldsymbol{\phi}_s = \mathbf{f}_{\varphi s}, \tag{40}$$

where the subscripts *a* and *s* represent the terms associated with the actuator and sensor, respectively.

Using the feedback control law [43], $\boldsymbol{\phi}_a$ is expressed as

$$\boldsymbol{\phi}_a = G_d \boldsymbol{\phi}_s + G_v \dot{\boldsymbol{\phi}}_s, \tag{41}$$

where G_d and G_v are the displacement and velocity feedback control gain, respectively.

For the sensor layer, it is assumed that there is no external charge $\mathbf{f}_{\varphi s}$, ignoring the converse piezoelectric effect. From (40), the voltage generated on the sensor layer can be defined as

$$\boldsymbol{\phi}_s = \mathbf{K}_{\varphi\varphi s}^{-1} \mathbf{K}_{\varphi us} \mathbf{d}_s. \tag{42}$$

From (41), (42), and (39), the charge of the actuator layer can be derived by

$$\mathbf{f}_{\varphi a} = \mathbf{K}_{\varphi ua} \mathbf{d}_a - G_d \mathbf{K}_{\varphi\varphi a} \mathbf{K}_{\varphi\varphi s}^{-1} \mathbf{K}_{\varphi us} \mathbf{d}_s - G_v \mathbf{K}_{\varphi\varphi a} \mathbf{K}_{\varphi\varphi s}^{-1} \mathbf{K}_{\varphi us} \dot{\mathbf{d}}_s. \tag{43}$$

From (43) and (37), the governing equation is rewritten as

$$\mathbf{M}_{uu} \ddot{\mathbf{d}} + (\mathbf{C}_R + \mathbf{C}) \dot{\mathbf{d}} + \bar{\mathbf{K}} \mathbf{d} = \mathbf{F}, \tag{44}$$

in which

$$\bar{\mathbf{K}} = \mathbf{K}_{uu} + G_d \mathbf{K}_{\varphi\varphi a} \mathbf{K}_{\varphi\varphi s}^{-1} \mathbf{K}_{\varphi us}, \tag{45}$$

and the active damping matrix \mathbf{C} is

$$\mathbf{C} = G_v \mathbf{K}_{\varphi\varphi a} \mathbf{K}_{\varphi\varphi s}^{-1} \mathbf{K}_{\varphi us}. \tag{46}$$

4. Numerical Results

The order of the NURBS basis functions should be equal to or greater than two to satisfy the requirement of C^1 continuity in approximate formulations [44]. Hence, the orders of the 2D NURBS basis functions in this study are set to be three ($p = q = 3$). For convenience, the plate’s mechanical boundary conditions are simplified as S, C, and F, where S represents the simply supported edge, with C and F representing the clamped edge and free edge, respectively. The dynamic responses and active vibration analysis of the plate are calculated via the Newmark- β direct integration method.

4.1. Convergence and Verification Studies

The convergence of the present method is verified via the calculation of the natural frequencies of a SSSS square PFGP. The dimensions of the PFGP as depicted in Figure 1 are: $a = b = 400$ mm,

$h_f = 5$ mm, and $h_p = 0.1$ mm. The materials of FGP and piezoelectric layer are Ti-6Al-4V/aluminum oxide and PZT-G1195N. All the material properties are displayed in Table 1.

Table 1. Material parameters.

Parameters	FGMs				Piezoelectric Materials
	Ti-6Al-4V	Aluminum Oxide	Al	Al ₂ O ₃	PZT-G1195N
	Young's modulus (Gpa)				
E_{11}	105.70	320.24	70	380	63.0
E_{22}	105.70	320.24	70	380	63.0
E_{33}	105.70	320.24	70	380	63.0
G_{12}	-	-	-	-	24.2
G_{13}	-	-	-	-	24.2
G_{23}	-	-	-	-	24.2
	Poisson's ratio				
ν_{12}	0.2981	0.26	0.3	0.3	0.3
ν_{13}	0.2981	0.26	0.3	0.3	0.3
ν_{23}	0.2981	0.26	0.3	0.3	0.3
	Density (kg/m ³)				
ρ	4429	3750	2707	3800	7600
	Piezoelectric coefficients (m/V)				
d_{31}	-	-	-	-	254×10^{-12}
d_{32}	-	-	-	-	254×10^{-12}
	Dielectric constant (F/m)				
k_{11}	-	-	-	-	15.3×10^{-9}
k_{22}	-	-	-	-	15.3×10^{-9}
k_{33}	-	-	--	--	15.0×10^{-9}

The four different control meshes of 10×10 , 12×12 , 16×16 , and 18×18 are shown in Figure 4. Table 2 lists the lowest 10 natural frequencies of the plate. It is seen that the natural frequencies calculated with the 16×16 mesh match well with the analytical solutions [45]. Furthermore, the effects on the natural frequency of each mode are not significant when the mesh level is greater than 16×16 . As a result, the 16×16 mesh and cubic NURBS basis functions are applied to all numerical subsequent examples. Figure 5 shows the first six mode shapes of the PFGP with a gradient index $n = 2$.

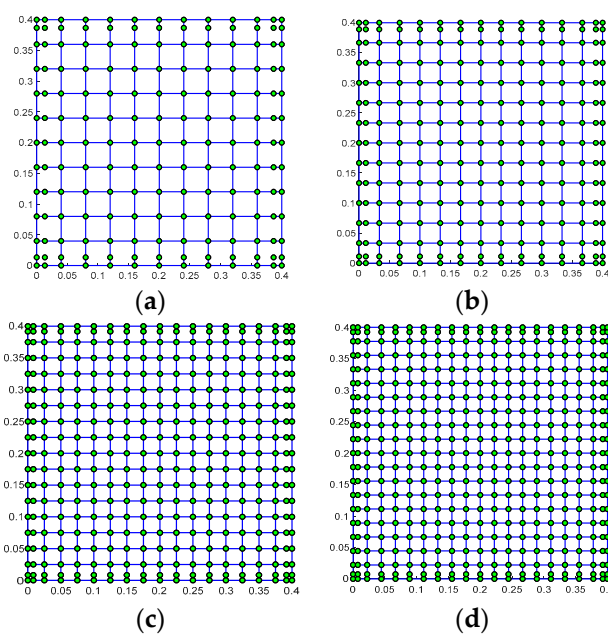


Figure 4. Four different control meshes of a square piezoelectric functionally graded plate (PFGP) with a fully simply supported boundary: (a) 10×10 ; (b) 12×12 ; (c) 16×16 ; (d) 18×18 .

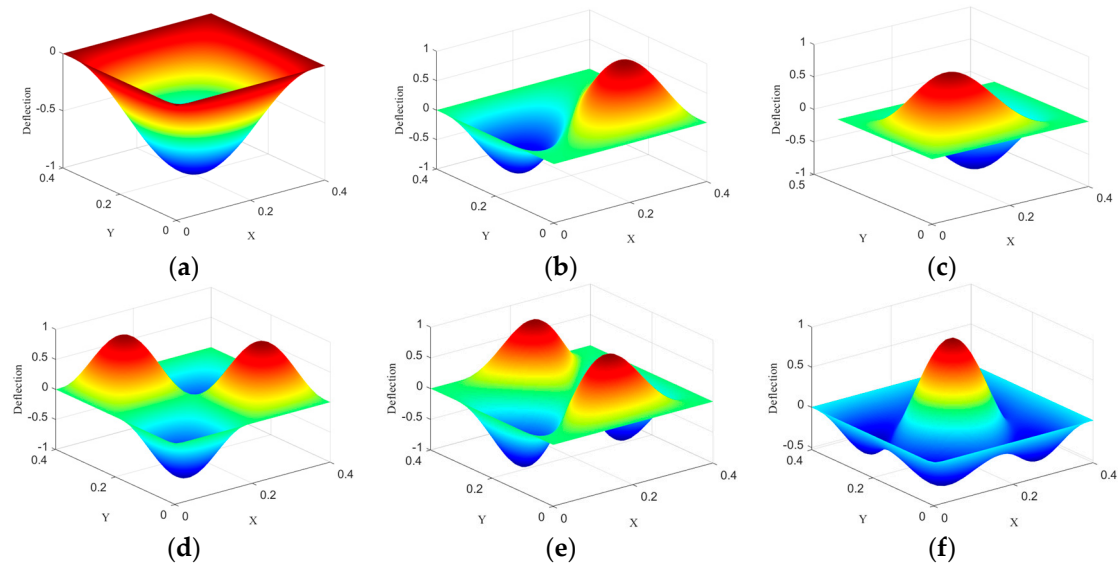


Figure 5. First six mode shapes of a simply supported PFGP: (a) Mode 1; (b) Mode 2; (c) Mode 3; (d) Mode 4; (e) Mode 5; (f) Mode 6.

Table 2. The lowest 10 natural frequencies (Hz) of a SSSS PFGP with different control meshes.

Mode	Method	<i>n</i>						
		0	0.5	1	5	15	100	1000
1	IGA (10 × 10)	145.355	186.550	200.615	232.411	249.284	261.318	263.696
	IGA (12 × 12)	145.355	186.550	200.615	232.411	249.283	261.317	263.695
	IGA (16 × 16)	145.355	186.550	200.614	232.410	249.283	261.317	263.695
	IGA (18 × 18)	145.355	186.550	200.614	232.410	249.283	261.317	263.695
	[45]	145.350	186.254	200.569	233.036	250.327	262.674	265.114
2/3	IGA (10 × 10)	363.085	466.002	501.155	580.604	622.741	652.785	658.721
	IGA (12 × 12)	363.070	465.982	501.133	580.581	622.716	652.759	658.695
	IGA (16 × 16)	363.061	465.970	501.119	580.566	622.701	652.743	658.678
	IGA (18 × 18)	363.060	465.968	501.117	580.563	622.698	652.740	658.676
	[45]	363.050	465.223	500.994	582.112	625.288	656.108	662.201
4	IGA (10 × 10)	580.400	744.936	801.160	928.208	995.551	1043.553	1053.035
	IGA (12 × 12)	580.382	744.911	801.132	928.178	995.520	1043.520	1053.001
	IGA (16 × 16)	580.371	744.895	801.115	928.160	995.500	1043.500	1052.981
	IGA (18 × 18)	580.369	744.893	801.112	928.160	995.497	1043.496	1052.977
	[45]	580.350	743.699	800.911	930.617	999.616	1048.857	1058.589
5/6	IGA (10 × 10)	725.405	931.104	1001.409	1160.205	1244.348	1304.318	1316.163
	IGA (12 × 12)	725.196	930.812	1001.091	1159.861	1243.988	1303.943	1315.785
	IGA (16 × 16)	725.073	930.640	1000.904	1159.658	1243.766	1303.721	1315.561
	IGA (18 × 18)	725.052	930.612	1000.873	1159.624	1243.741	1303.685	1315.524
	[45]	725.000	929.078	1000.571	1162.638	1248.819	1310.310	1322.461
7/8	IGA (10 × 10)	941.987	1209.114	1300.455	1506.753	1616.004	1693.840	1709.211
	IGA (12 × 12)	941.818	1208.877	1300.197	1506.741	1615.712	1693.536	1708.904
	IGA (16 × 16)	941.718	1208.738	1300.047	1506.310	1615.540	1693.357	1708.723
	IGA (18 × 18)	941.702	1208.716	1300.022	1506.283	1615.512	1693.327	1708.694
	[45]	941.640	1206.740	1299.640	1510.197	1622.102	1701.923	1717.694
9/10	IGA (10 × 10)	1232.501	1582.351	1702.018	1971.842	2114.649	2216.399	2236.490
	IGA (12 × 12)	1231.079	1580.332	1699.815	1969.482	2112.191	2213.838	2233.907
	IGA (16 × 16)	1230.273	1579.200	1698.580	1968.149	2110.799	2212.388	2232.444
	IGA (18 × 18)	1230.145	1579.021	1698.386	1967.938	2110.579	2212.158	2232.212
	[45]	1229.880	1576.201	1697.617	1972.734	2118.843	2223.021	2243.603

4.2. Free Vibration Analysis

For investigating the effects of the electrical boundary conditions on natural frequencies of the PFGP, a SSSS PFGP with different ratios of h_f/a and h_p/h_f is taken into consideration for comparison. In the closed circuit, two piezoelectric layers are both grounded, while in the open circuit, the electric potential remains free, which implies that there is no electric displacement. The materials of PFGP are Al/Al₂O₃ and PZT-4, and the material parameters of PZT-4 are defined in [45]. Note that, in this example, $n = 0$ means that the FGP consists only of ceramic (Al₂O₃). Conversely, $n = \infty$ means that the FGP is an isotropic metal (Al) plate. Table 3 lists the natural frequencies of the plate with different dimension scales. Besides, Table 4 shows the lowest six natural frequencies of a square plate with SSSC and SCSC boundary conditions when $h_f/a = 0.02$ and $h_p/h_f = 0.1$. It can be seen that the results from the S-FSDT-based IGA match well with those of the analytical [45] and numerical [25] solutions.

Table 3. The lowest two natural frequencies (Hz) of a SSSS PFGP with open and closed circuits.

h_f/a	h_p/h_f	Electrical Condition	Mode	$n = 0$		$n = 0.5$		$n = 1$	
				Present	[45]	Present	[45]	Present	[45]
0.05	0.1	Closed	1	426.704	426.662	369.050	369.015	339.888	339.859
			2	1049.687	1049.356	908.204	907.918	836.293	836.020
	Open	1	433.793	433.747	377.971	377.934	350.126	350.092	
		2	1066.743	1066.390	929.708	929.406	860.967	860.669	
	0.2	Closed	1	408.435	408.475	362.207	362.269	340.242	340.311
			2	1001.350	1001.133	887.808	887.637	833.442	833.266
Open	1	421.961	421.983	378.417	378.460	358.168	358.212		
	2	1033.682	1033.381	926.547	926.311	876.222	875.953		
0.1	0.1	Closed	1	826.873	826.463	715.679	715.319	658.905	658.555
			2	1954.769	1952.530	1694.005	1691.992	1558.808	1556.838
	Open	1	840.030	839.595	732.294	731.920	677.970	677.597	
		2	1983.671	1981.321	1730.703	1728.702	1600.948	1598.821	
	0.2	Closed	1	786.393	786.011	697.081	696.730	654.023	653.652
			2	1841.071	1838.475	1630.952	1628.388	1527.467	1524.747
Open	1	811.198	810.723	726.796	726.393	686.798	686.343		
	2	1894.719	1891.714	1695.063	1692.715	1598.083	1595.292		

Table 4. The natural frequencies (Hz) of SSSC and SCSC PFGPs.

n	Mode	Boundary Conditions							
		SSSC				SCSC			
		Open Circuit		Closed Circuit		Open Circuit		Closed Circuit	
	Present	[25]	Present	[25]	Present	[25]	Present	[25]	
0	1	209.750	208.651	206.281	205.550	256.565	254.251	252.330	251.120
	2	457.219	454.822	449.683	448.463	484.164	480.640	476.190	474.440
	3	518.331	513.724	509.805	507.453	611.731	602.687	601.699	596.858
	4	759.533	751.930	747.075	743.357	833.053	821.085	819.420	813.141
	5	883.305	876.924	868.834	866.929	900.225	892.760	885.483	882.944
	6	995.360	982.452	979.117	973.305	1131.713	1109.422	1113.343	1101.578
1	1	169.301	168.200	164.296	163.727	207.096	204.560	200.984	200.041
	2	369.044	366.401	358.167	357.223	390.797	386.889	379.288	377.936
	3	418.385	413.303	406.077	404.247	493.802	483.968	493.318	475.541
	4	613.063	604.586	595.075	592.200	672.432	659.364	652.744	647.876
	5	712.952	705.039	692.056	690.600	726.615	717.565	705.327	703.381
	6	803.453	788.691	779.993	775.467	913.608	889.211	887.063	877.852
15	1	147.106	145.798	140.782	140.155	179.859	176.792	172.147	171.103
	2	320.364	317.022	306.656	305.467	339.173	334.267	324.677	323.006
	3	362.992	356.745	347.506	345.368	428.071	416.219	409.888	405.664
	4	531.147	520.850	508.885	505.316	582.586	566.509	557.909	552.131
	5	617.872	607.441	591.657	589.345	629.633	617.822	602.937	600.054
	6	695.567	677.205	666.222	660.679	789.825	760.509	756.752	746.359
1000	1	132.128	130.883	125.082	124.591	161.553	158.500	152.959	152.151
	2	287.775	284.556	272.499	271.659	304.677	299.892	288.521	287.316

3	326.083	319.956	308.822	307.247	384.572	372.904	364.300	361.092
4	477.475	467.118	452.296	449.750	523.425	507.747	495.908	491.650
5	555.120	544.766	525.892	524.530	565.693	554.003	535.927	534.127
6	624.981	606.883	592.251	588.375	709.757	681.066	672.853	665.183

4.3. Static Bending Analysis

A cantilevered (CFFF) square PFGP with the same materials and dimensions as those in Section 4.1 is used for analyzing the static bending responses.

First, the centerline deflection of the plate under a uniformly distributed load of -100 N/m^2 is displayed in Figure 6. The deflection obviously decreases when n increases due to the increase in the elastic modulus value $E(z)$ of the FGP.

Next, the centerline deflection of the plate under a 10 V voltage is plotted in Figure 7. This situation involves the open-loop control of the plate, in which both two piezoelectric layers act as actuators. In this situation, the upper piezoelectric layer is polarized in the direction of the applied electric field, and the lower piezoelectric layer is polarized in the opposite direction of the applied electric field. In the case of the converse piezoelectric effect, the upper piezoelectric layer contracts, while the lower piezoelectric layer extends along the direction of the length.

The centerline deflection of the plate under a uniformly distributed load of -100 N/m^2 and different input electric voltages is shown in Figure 8. It can be observed that the deflection decreases as the input voltages increase. Meanwhile, Table 5 lists the tip deflection values of the plate. The results in this approach are in good agreement with the solutions in [15].

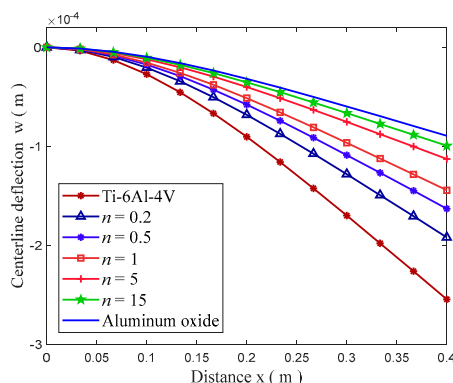


Figure 6. Deflection of a cantilevered PFGP with different gradient index n under the action of a uniformly distributed load.

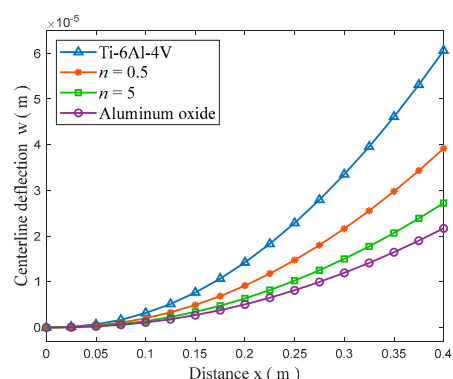


Figure 7. Deflection of a cantilevered PFGP under an input voltage of 10 V with different n .

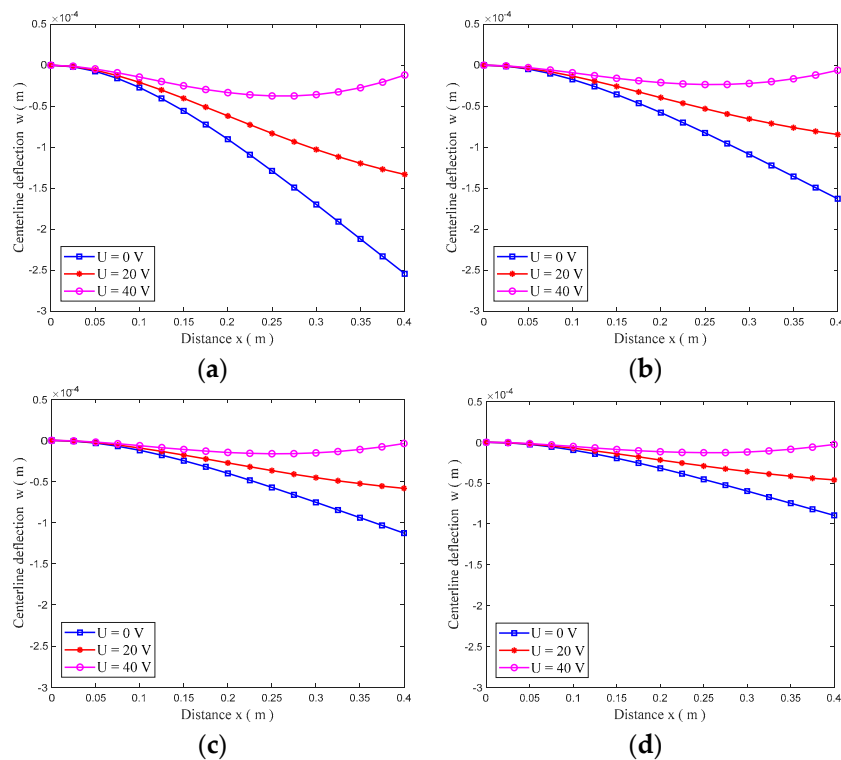


Figure 8. Deflection of a PFGP under the action of electromechanical loads: (a) $n = 0$; (b) $n = 0.5$; (c) $n = 5$; (d) $n = \infty$.

We also investigated the bending response of PFGPs which are subjected to the voltage range 0–60 V with different mechanical boundary conditions. Figure 9 provides the tip deflection or central node deflection of the plate with $n = 2$. It is observed that the deflections increase linearly with the increase in the voltage. For the CFFF plate, the deflection is positive, while for the other boundary conditions, the deflections are negative. This phenomenon is due to the upper piezoelectric layer being shortened and the lower piezoelectric layer being elongated due to the converse piezoelectric effect. At the same time, the change of mechanical boundary conditions also results in the change of the deflection direction of the plate.

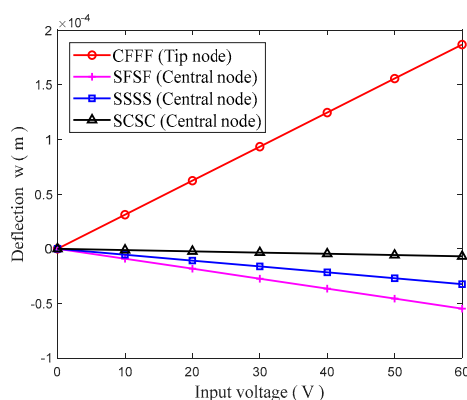


Figure 9. Deflection of a PFGP with different boundary conditions.

Table 5. Tip deflection of a CFFF PFGP under the action of electromechanical loads (10^{-4} m).

n	Method	Input Electric Voltages (V)		
		0	20	40
$n = 0$	[15]	−2.5460	−1.3346	−0.1232
	Present	−2.5433	−1.3323	−0.1212
$n = 0.5$	[15]	−1.6199	−0.8440	−0.0681

$n = 5$	Present	-1.6167	-0.8421	-0.0675
	[15]	-1.1266	-0.5820	-0.0375
$n = \infty$	Present	-1.1253	-0.5811	-0.0369
	[15]	-0.8947	-0.4609	-0.0271
	Present	-0.8939	-0.4602	-0.0265

4.4. Dynamic analysis

A SSSS square FGP (Al/Al₂O₃) with $n = 1$ is used for demonstrating the validity of the dynamic analysis with the S-FSDT-based IGA. The length and thickness of the plate are 200 mm and 10 mm. Four different distributed transverse forces are defined as

$$q = q_0 \sin\left(\frac{\pi x}{a}\right) \sin\left(\frac{\pi y}{b}\right) F(t) \tag{47}$$

in which $q_0 = -15$ Mpa, and $F(t)$ is defined as

$$F(t) = \begin{cases} \begin{cases} 1 & \text{Step load} \\ 1-t/t_1 & \text{Triangular load} \\ \sin(\pi t/t_1) & \text{Sinusoidal load} \\ e^{-\bar{\gamma}t} & \text{Explosive load} \end{cases} & \text{if } 0 \leq t \leq t_1 \\ 0 & \text{if } t \geq t_1 \end{cases} \tag{48}$$

where $\bar{\gamma} = 330s^{-1}$ and $t_1 = 0.003$ s.

The normalized central transient deflection $\bar{w} = w/h$ of the plate under the action of sinusoidal load is depicted in Figure 10. Apparently, the results of this study coincide with those in [46].

Next, a SSSS plate with sizes of $a = b = 200$ mm, $h_p = 2$ mm, and $h_f = 20$ mm was selected to study the dynamic response of PFGP. The FGM constituents are Ti-6Al-4V and aluminum oxide. The piezoelectric material is PZT-G1195N.

Introducing Rayleigh damping, Figure 11 shows the transient deflections of the plate. It is observed that the vibration amplitude and period of motions decrease with the increase in the gradient index n due to the strengthening of stiffness of the plate.

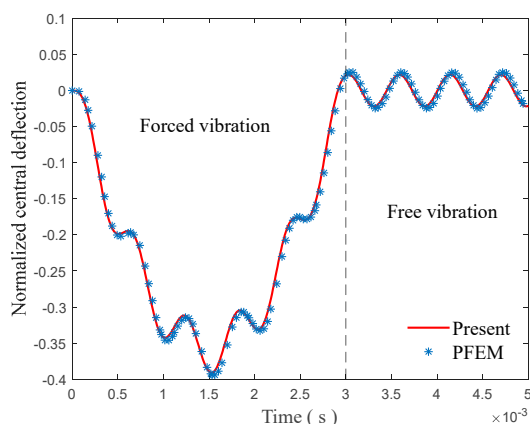


Figure 10. Transient normalized central deflection of a SSSS FGP with $n = 1$.

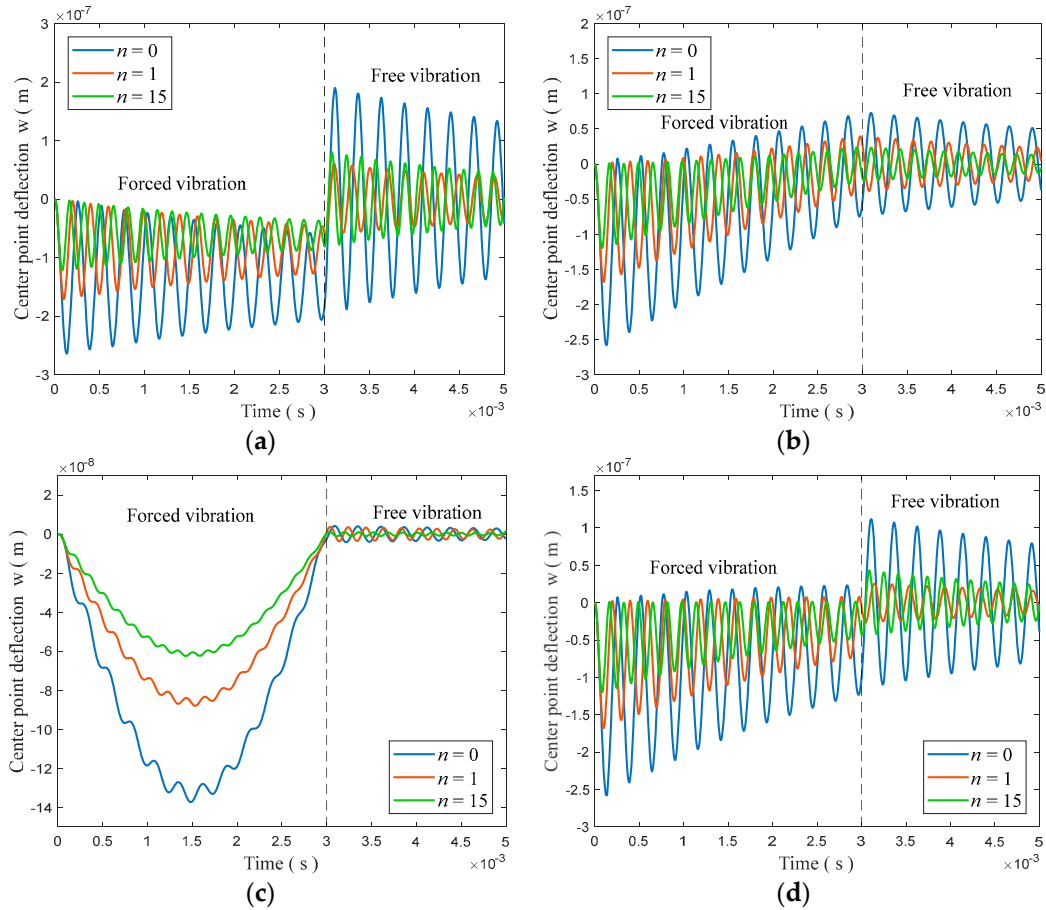
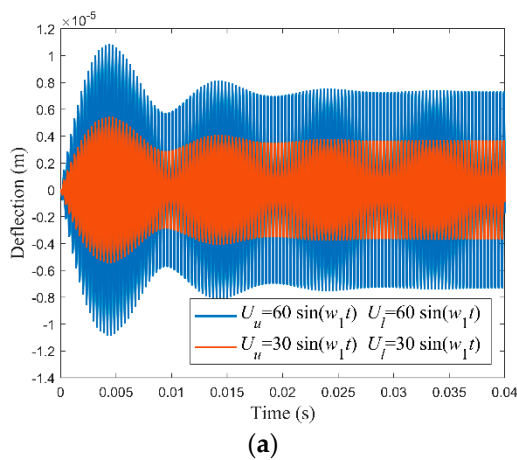


Figure 11. Dynamic analysis of a simply supported (SSSS) PFGP under four different sinusoidally distributed transverse forces: (a) Step load; (b) triangular load; (c) sinusoidal load; (d) explosive load.

Next, we analyze the dynamic response of PFGPs with $n=2$ under the time-varying electric loads. As shown in Figure 12, the magnitude of the voltage amplitude U_0 will affect the vibration amplitude of the plate. Due to the effect of structural damping, the central vibration amplitude of the plate tends to be stable after a period of time. In this example, the time step is set to be $2\pi/(20w_1)$, in which w_1 is the first natural frequency (rad/s) of the plate.



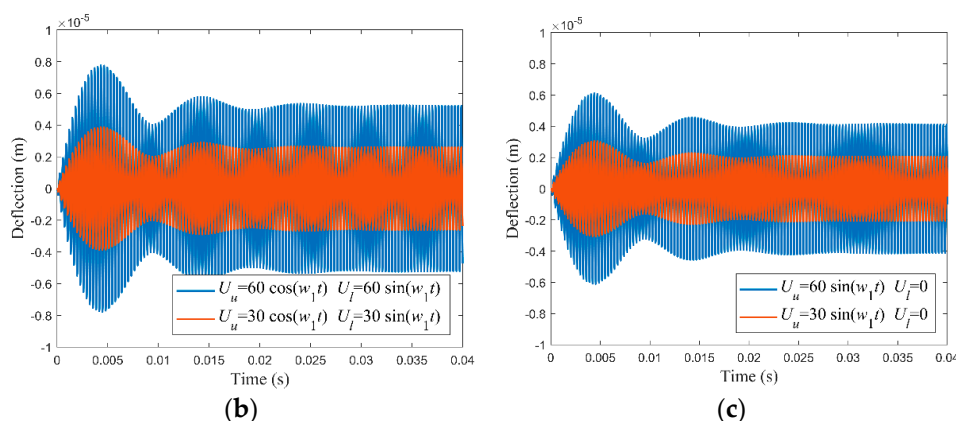


Figure 12. Transient analysis of a simply supported (SSSS) PFGP when the upper and lower piezoelectric layers are subjected to voltage loads: (a) $U_u = U_l = U_0 \sin(w_1 t)$; (b) $U_u = U_0 \cos(w_1 t)$, $U_l = U_0 \sin(w_1 t)$; (c) $U_u = U_0 \sin(w_1 t)$, $U_l = 0$.

4.5. Active Control Analysis

A square plate and a clamped circular plate are applied for the static bending control analysis and dynamic vibration control analysis of the FGP through piezoelectric actuators and sensors. The materials of the FGP and piezoelectric layers in this section are Ti-6Al-4V/aluminum oxide and PZT-G1195N.

4.5.1. Static Bending Control

1. Square plate

A square PFGP with $n = 2$ and SSSS and CFFF boundary conditions is used for investigating the static bending control. The dimensions of the plate are set as: $a = b = 300$ mm, $h_p = 0.1$ mm, and $h_f = 5$ mm. The effects of the displacement feedback control gain G_d on the plate’s static bending response under a uniformly distributed load of $q = -100$ N/m² are plotted in Figure 13. As expected, the centerline deflections of the plates decrease with the increase in the gain G_d .

2. Circular plate

A clamped circular PFGP with $n = 2$ is also considered. The thicknesses of the plate and each piezoelectric layer are 0.3 mm and 0.05 mm. The radius R is 50 mm. Figure 14 shows the deformation of the plate under a mechanical load of -100 N/m². We can see that the deformation of the circular plate can also be effectively controlled by G_d .

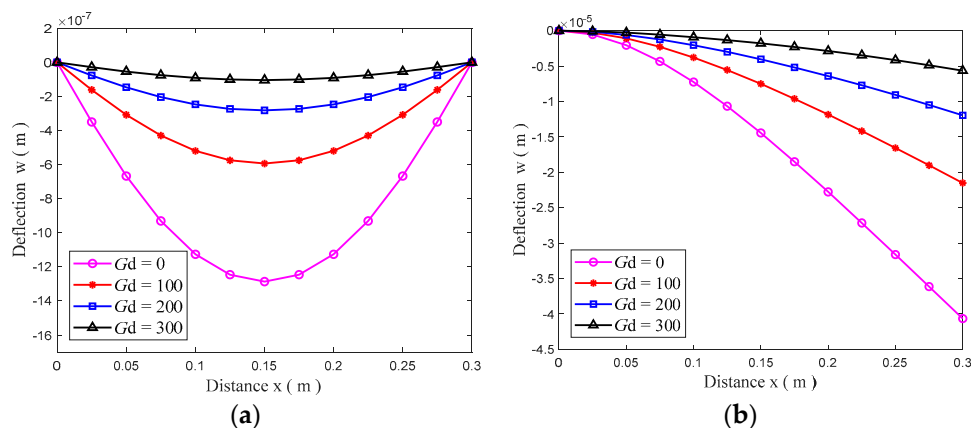


Figure 13. Static bending control of FGP through the gain G_d : (a) a SSSS plate; (b) a CFFF plate.

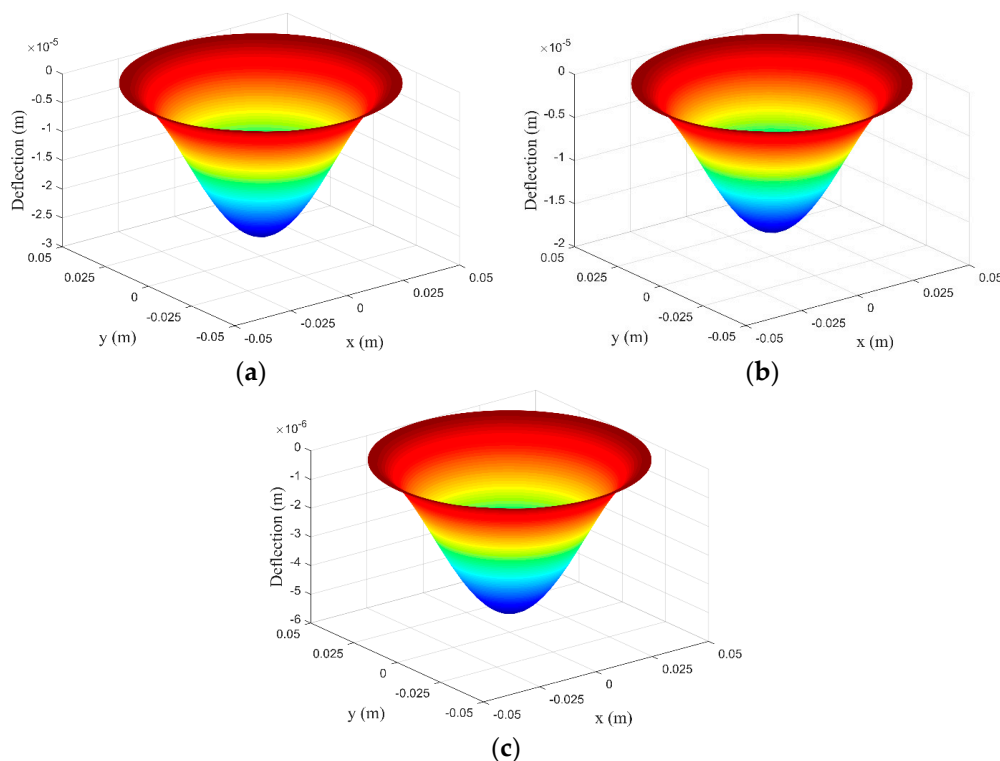


Figure 14. Static bending control of a circular PFGP through the displacement feedback control gain: (a) $G_d = 0$; (b) $G_d = 5$; (c) $G_d = 20$.

4.5.2. Dynamic Vibration Control

1. Square plate

First, we assume that the former square CFFF PFGP is initially subjected to a downward uniformly distributed load of -100 N/m^2 , then the load is instantaneously removed, resulting in the motion from the initial displacement. The piezoelectric stress constants e_{31} and e_{32} are 6.1468 C/m^2 , and the Rayleigh damping C_R of the plate is not considered in this example.

If the stretching–bending coupling effect exists, the active damping C ($C = G_v K_{\varphi\varphi a} K_{\varphi\varphi s}^{-1} K_{\varphi u s}$) is not a symmetric positive definite matrix [25,47]. As shown in Figure 15, the dynamic vibration control of plate structures with piezoelectric layers symmetrically distributed on the upper and lower surfaces may be unstable. The main purpose of introducing the neutral surface in this paper is to solve the instability of dynamic vibration control for this sort of plate structure.

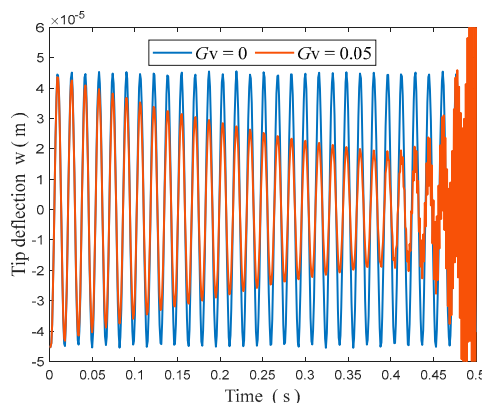


Figure 15. Tip deflection of a cantilevered plate with $n = 1$ by using a geometric middle surface.

Figure 16 shows the transient deflection response at the tip of the PFGP with $n = 0$ and $n = \infty$ by using the neutral surface. It is clear that the vibration response attenuates faster when the control

gain G_v increases and the results match well with the mesh-free method presented by Selim et al. [25]. It is noteworthy that the stretching–bending coupling effect does not exist when $n=0$ and $n=\infty$. Similarly, Figure 17 depicts the transient deflection of the PFGP with $n=1$ and $n=15$, and we can see that the dynamic vibration control effect is still stable.

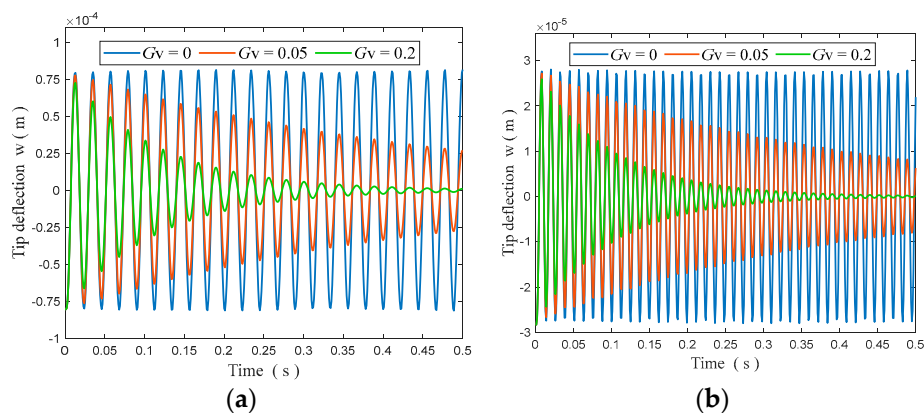


Figure 16. The tip transient deflection of a CFFF PFGP under an initial uniformly distributed load of -100 N/m^2 : (a) $n = 0$; (b) $n = \infty$.

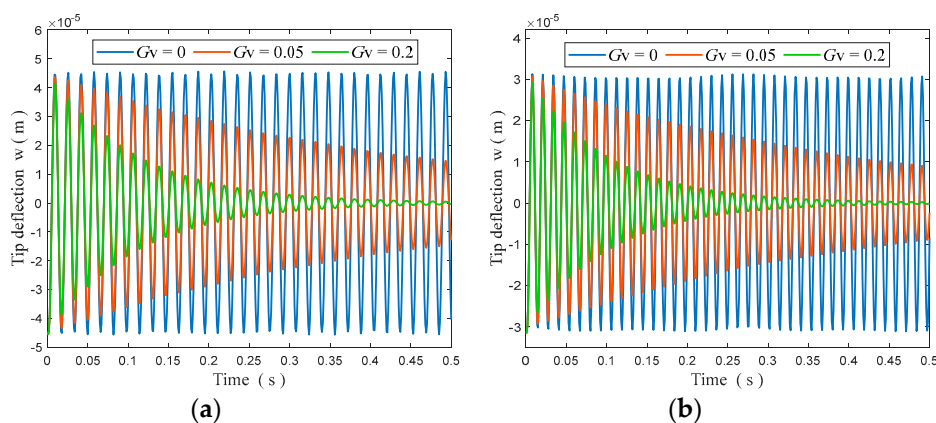


Figure 17. The tip transient deflection of a CFFF PFGP under an initial uniformly distributed load of -100 N/m^2 : (a) $n = 1$; (b) $n = 15$.

Next, a fully clamped (CCCC) square PFGP is used for studying the active vibration control under four different sinusoidally distributed transverse forces defined in (47) with $q_0 = -1 \times 10^4 \text{ N/m}^2$. The length of the plate is 200 mm, and the thicknesses of the FGP and each piezoelectric layer are 20 mm and 2 mm, respectively.

The transient deflection responses of the central point with different control gains are plotted in Figure 18. Similarly, in both the forced vibration state and free vibration state, the oscillation is significantly suppressed when the control gain G_v increases.

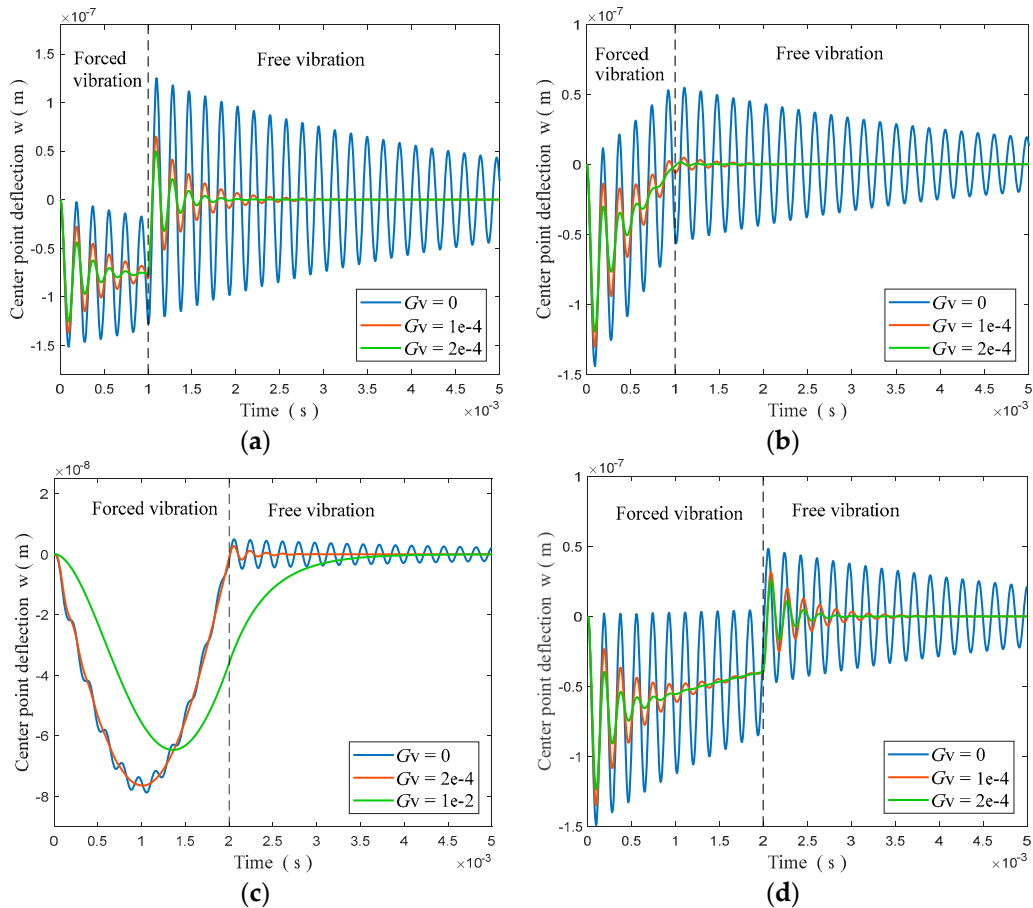


Figure 18. Transient deflection responses of a CCC PFGP under four different time-varying loads: (a) Step load; (b) triangular load; (c) sinusoidal load; (d) explosive load.

2. Circular plate

The circular plate in the section of static bending control is used for further investigation. With the action of an initial uniformly distributed load of -100 N/m^2 , the time of vibration attenuation to the weakest is investigated in Figure 19. It is observed that the decay time decreases with the increase of n , and the larger the value of G_v , the faster the vibration disappears.

Based on the above analysis, we can conclude that the static deformation and the vibration of FGP can be effectively controlled by using the displacement feedback control gain G_d and the velocity feedback control gain G_v . By using this feature, controllers can be designed and optimized according to the requirements of different applications to control both the displacement and oscillation time.

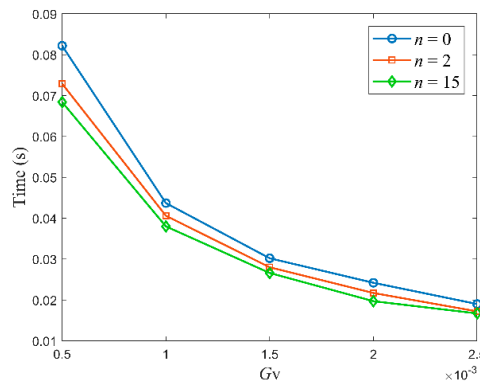


Figure 19. Time of vibration attenuation to the weakest with different G_v .

5. Conclusions

In this study, an isogeometric analysis method (IGA) based on a simple first-order shear deformation theory (S-FSDT) was used for investigating the free vibration, static bending response, dynamic response, and active control analysis of FGPs with surface-bonded piezoelectric actuators and sensors. Through some numerical examples, several major points can be drawn as follows:

- ◆ The isogeometric finite element motion equations of piezoelectric functionally graded plates (PFGPs) based on the simple first-order shear deformation theory can be derived easily, due to one unknown saved in S-FSDT.
- ◆ From some comparison studied of free vibration and static bending analyses of piezoelectric functionally graded plates, it can be obtained that although one unknown is saved in simple first-order shear deformation theory, the S-FSDT-based IGA method is still effective and accurate.
- ◆ Due to the electromechanical coupling effect, the natural frequencies of the piezoelectric functionally graded plates in open-circuit state are greater than those in closed-circuit state.
- ◆ The vibration amplitude tends to be stable after a period of time when the plate is subjected to time-varying electric loads; the greater the amplitude of the voltage, the greater the amplitude of the vibration.
- ◆ For closed-loop control analysis of the plates, the static bending response can be altered by adjusting the displacement feedback control gain G_d , and the dynamic vibration and vibration time can be controlled through the velocity feedback control gain G_v .

Author Contributions: Conceptualization, T.L.; methodology, C.W.; software, T.L. and C.W.; validation, C.L., J.W.L. and K.H.C.; formal analysis, T.L.; investigation, K.H.C.; resources, C.W.; data curation, C.L.; writing—original draft preparation, T.L.; writing—review and editing, T.L. and K.H.C. All authors have read and agreed to the published version of the manuscript.

Funding: This research was funded by University Synergy Innovation Program of Anhui Province, grant number GXXT-2019-04, National Key Technologies Research & Development Program of China, grant number 2017YFC0805100, Scientific Research Foundation of Education Department of Anhui Province, grant numbers KJ2018A0069, KJ2019A0091 and Singapore University of Technology and Design, grant numbers SRG SCI 2019 142.

Conflicts of Interest: The authors declare no conflict of interest

Nomenclature

a	Plate length	\mathbf{N}	In-plane forces
b	Plate width	\mathbf{M}	Moments
h_t	Total thickness of the plate	\mathbf{P}	Shear forces
h_f	Thickness of the FGM layer	f_z	Transverse mechanical surface load
h_p	Thickness of each piezoelectric layer	\mathbf{M}^P	Moments generated by electric field
P	Material properties of FGM	\mathbf{B}_φ	Relation matrix between electric field and electric potential
P_m	Material properties of metal constituent	\mathbf{d}	Displacement vector after assembling the elements
P_c	Material properties of ceramic constituent	\mathbf{u}	Displacement vector
V_m	Volume fraction of metal	$\dot{\mathbf{u}}$	First time derivative of \mathbf{u}
n	Gradient index	\mathbf{q}_s	Surface charge
\mathbf{D}	Electrical displacement	\mathbf{f}_s	Surface loads
\mathbf{g}	Permittivity constant matrix	\mathbf{M}_{uu}	Mass matrix
z_0	Distance between the mid and neutral surfaces	$\ddot{\mathbf{d}}$	Second time derivative of \mathbf{d}

$\tilde{\epsilon}$	Geometric strain	$\dot{\mathbf{d}}$	First time derivative of \mathbf{d}
ϵ	In-plane strains	\mathbf{E}	Electric field
γ	Shear strains	$\mathbf{K}_{\varphi\varphi}$	Electric stiffness matrix
β_x	Rotations of a transverse normal about the y axis	\mathbf{N}^P	In-plane forces generated by electric field
β_y	Rotations of a transverse normal about the x axis	q_E	Charge density on the surface of piezoelectric layer
\mathbf{e}	Piezoelectric stress constant matrix	\mathbf{C}	Active damping matrix
\mathbf{Q}_p	Elastic constant of piezoelectric materials	\mathbf{C}_R	Rayleigh damping
\mathbf{Q}_f	Elastic constant of FGM	α_R, β_R	Rayleigh damping factors
k	Shear correction factor	G_d	Displacement feedback control gain
$\vartheta_{i,j}$	Weight	G_v	Velocity feedback control gain
G, H	B-spline basis functions	$\mathbf{K}_{u\varphi}, \mathbf{K}_{\varphi u}$	Displacement-electric stiffness matrices
p, q	Orders of B-spline basis functions	Φ_k	Nodal electric potential vector
\mathbf{d}_k	Displacement vector of control point k	\mathbf{K}_{uu}	Stiffness matrix

References

- Zenkour, A.; Hafed, Z.S.; Radwan, A.F. Bending Analysis of Functionally Graded Nanoscale Plates by Using Nonlocal Mixed Variational Formula. *Mathematics* **2020**, *8*, 1162, doi:10.3390/math8071162.
- Sobczak, J.J.; Drenchev, L. Metallic Functionally Graded Materials: A Specific Class of Advanced Composites. *J. Mater. Sci. Technol.* **2013**, *29*, 297–316, doi:10.1016/j.jmst.2013.02.006.
- Li, Y.-D.; Tang, Z.-C.; Fu, Z.-J. Generalized Finite Difference Method for Plate Bending Analysis of Functionally Graded Materials. *Mathematics* **2020**, *8*, 1940, doi:10.3390/math8111940.
- Tran, L.V.; Thai, C.H.; Nguyen-Xuan, H. An isogeometric finite element formulation for thermal buckling analysis of functionally graded plates. *Finite Elem. Anal. Des.* **2013**, *73*, 65–76, doi:10.1016/j.finela.2013.05.003.
- He, X.-T.; Yang, Z.-X.; Li, Y.-H.; Li, X.; Sun, J.-Y. Application of Multi-Parameter Perturbation Method to Functionally-Graded, Thin, Circular Piezoelectric Plates. *Mathematics* **2020**, *8*, 342, doi:10.3390/math8030342.
- Milazzo, A.; Orlando, C. An equivalent single-layer approach for free vibration analysis of smart laminated thick composite plates. *Smart Mater. Struct.* **2012**, *21*, 75031, doi:10.1088/0964-1726/21/7/075031.
- Yiqi, M.; Yiming, F. Nonlinear dynamic response and active vibration control for piezoelectric functionally graded plate. *J. Sound Vib.* **2010**, *329*, 2015–2028, doi:10.1016/j.jsv.2010.01.005.
- Jadhav, P.A.; Bajoria, K.M. Buckling of piezoelectric functionally graded plate subjected to electro-mechanical loading. *Smart Mater. Struct.* **2012**, *21*, 105005, doi:10.1088/0964-1726/21/10/105005.
- Ray, M.; Sachade, H. Finite element analysis of smart functionally graded plates. *Int. J. Solids Struct.* **2006**, *43*, 5468–5484, doi:10.1016/j.ijsolstr.2005.06.096.
- Loja, M.A.R.; Soares, C.M.M.; Barbosa, J. Analysis of functionally graded sandwich plate structures with piezoelectric skins, using B-spline finite strip method. *Compos. Struct.* **2013**, *96*, 606–615, doi:10.1016/j.compstruct.2012.08.010.
- He, X.; Ng, T.; Sivashanker, S.; Liew, K. Active control of FGM plates with integrated piezoelectric sensors and actuators. *Int. J. Solids Struct.* **2001**, *38*, 1641–1655, doi:10.1016/s0020-7683(00)00050-0.
- Liew, K.; He, X.Q.; Ng, T.Y.; Sivashanker, S. Active control of FGM plates subjected to a temperature gradient: Modelling via finite element method based on FSDT. *Int. J. Numer. Methods Eng.* **2001**, *52*, 1253–1271, doi:10.1002/nme.252.
- Liew, K.; Sivashanker, S.; He, X.Q.; Ng, T.Y. The modelling and design of smart structures using functionally graded materials and piezoelectrical sensor/actuator patches. *Smart Mater. Struct.* **2003**, *12*, 647–655, doi:10.1088/0964-1726/12/4/316.
- Aryana, F.; Bahai, H.; Mirzaeifar, R.; Yeilaghi, A. Modification of dynamic characteristics of FGM plates with integrated piezoelectric layers using first- and second-order approximations. *Int. J. Numer. Methods Eng.* **2007**, *70*, 1409–1429, doi:10.1002/nme.1927.

15. Nguyen-Quang, K.; Dang-Trung, H.; Ho-Huu, V.; Luong-Van, H.; Nguyen-Thoi, T. Analysis and control of FGM plates integrated with piezoelectric sensors and actuators using cell-based smoothed discrete shear gap method (CS-DSG3). *Compos. Struct.* **2017**, *165*, 115–129, doi:10.1016/j.compstruct.2017.01.006.
16. Nguyen-Thoi, T.; Phung-Van, P.; Nguyen-Xuan, H.; Thai-Hoang, C. A cell-based smoothed discrete shear gap method using triangular elements for static and free vibration analyses of Reissner-Mindlin plates. *Int. J. Numer. Methods Eng.* **2012**, *91*, 705–741, doi:10.1002/nme.4289.
17. Fakhari, V.; Ohadi, A.; Yousefian, P. Nonlinear free and forced vibration behavior of functionally graded plate with piezoelectric layers in thermal environment. *Compos. Struct.* **2011**, *93*, 2310–2321, doi:10.1016/j.compstruct.2011.03.019.
18. Fakhari, V.; Ohadi, A. Nonlinear vibration control of functionally graded plate with piezoelectric layers in thermal environment. *J. Vib. Control.* **2010**, *17*, 449–469, doi:10.1177/1077546309354970.
19. Nguyen, N.V.; Lee, J.; Nguyen-Xuan, H. Active vibration control of GPLs-reinforced FG metal foam plates with piezoelectric sensor and actuator layers. *Compos. Part B Eng.* **2019**, *172*, 769–784, doi:10.1016/j.compositesb.2019.05.060.
20. Belinha, J.; Araújo, A.; Ferreira, A.J.M.; Dinis, L.; Natal, R.M. The analysis of laminated plates using distinct advanced discretization meshless techniques. *Compos. Struct.* **2016**, *143*, 165–179, doi:10.1016/j.compstruct.2016.02.021.
21. Sladek, J.; Stanak, P.; Han, Z.D.; Sladek, V.; Atluri, S.N. Applications of the MLPG method in engineering & sciences: A review. *Comput. Model Eng.* **2013**, *92*, 423–475.
22. Dai, K.; Liu, G.; Han, X.; Lim, K.-M. Thermomechanical analysis of functionally graded material (FGM) plates using element-free Galerkin method. *Comput. Struct.* **2005**, *83*, 1487–1502, doi:10.1016/j.compstruc.2004.09.020.
23. Chen, X.; Zhao, Z.; Liew, K. Stability of piezoelectric FGM rectangular plates subjected to non-uniformly distributed load, heat and voltage. *Adv. Eng. Softw.* **2008**, *39*, 121–131, doi:10.1016/j.advengsoft.2006.12.004.
24. Nourmohammadi, H.; Behjat, B. Geometrically nonlinear analysis of functionally graded piezoelectric plate using mesh-free RPIM. *Eng. Anal. Bound. Elem.* **2019**, *99*, 131–141, doi:10.1016/j.enganabound.2018.11.006.
25. Selim, B.; Zhang, L.; Liew, K. Active vibration control of FGM plates with piezoelectric layers based on Reddy's higher-order shear deformation theory. *Compos. Struct.* **2016**, *155*, 118–134, doi:10.1016/j.compstruct.2016.07.059.
26. Hughes, T.; Cottrell, J.; Bazilevs, Y. Isogeometric analysis: CAD, finite elements, NURBS, exact geometry and mesh refinement. *Comput. Methods Appl. Mech. Eng.* **2005**, *194*, 4135–4195, doi:10.1016/j.cma.2004.10.008.
27. Phung-Van, P.; Tran, L.V.; Ferreira, A.J.M.; Nguyen-Xuan, H.; Wahab, M.A. Nonlinear transient isogeometric analysis of smart piezoelectric functionally graded material plates based on generalized shear deformation theory under thermo-electro-mechanical loads. *Nonlinear Dyn.* **2017**, *87*, 879–894, doi:10.1007/s11071-016-3085-6.
28. Van, P.P.; De Lorenzis, L.; Thai, C.H.; Wahab, M.A.; Nguyen-Xuan, H. Analysis of laminated composite plates integrated with piezoelectric sensors and actuators using higher-order shear deformation theory and isogeometric finite elements. *Comput. Mater. Sci.* **2015**, *96*, 495–505, doi:10.1016/j.commatsci.2014.04.068.
29. Van, P.P.; Nguyen, L.B.; Tran, L.V.; Dinh, T.D.; Thai, C.H.; Bordas, S.; Wahab, M.A.; Nguyen-Xuan, H. An efficient computational approach for control of nonlinear transient responses of smart piezoelectric composite plates. *Int. J. Non-Linear Mech.* **2015**, *76*, 190–202, doi:10.1016/j.ijnonlinmec.2015.06.003.
30. Nguyen, L.B.; Nguyen, N.V.; Thai, C.H.; Ferreira, A.; Nguyen-Xuan, H. An isogeometric Bézier finite element analysis for piezoelectric FG porous plates reinforced by graphene platelets. *Compos. Struct.* **2019**, *214*, 227–245, doi:10.1016/j.compstruct.2019.01.077.
31. Nguyen-Quang, K.; Vo-Duy, T.; Dang-Trung, H.; Nguyen-Thoi, T. An isogeometric approach for dynamic response of laminated FG-CNT reinforced composite plates integrated with piezoelectric layers. *Comput. Methods Appl. Mech. Eng.* **2018**, *332*, 25–46, doi:10.1016/j.cma.2017.12.010.
32. Lv, Q.; Yao, Z.; Li, X. Contact analysis and experimental investigation of a linear ultrasonic motor. *Ultrasonics* **2017**, *81*, 32–38, doi:10.1016/j.ultras.2017.05.017.
33. Wang, G.; Li, C.; Yuan, T. Design and experiment of a small-scale walking robot employing stick-slip motion principle. *Rev. Sci. Instrum.* **2017**, *88*, 115001, doi:10.1063/1.4991063.
34. Trabelsi, S.; Frikha, A.; Zghal, S.; Dammak, F. A modified FSDT-based four nodes finite shell element for thermal buckling analysis of functionally graded plates and cylindrical shells. *Eng. Struct.* **2019**, *178*, 444–459, doi:10.1016/j.engstruct.2018.10.047.

35. Thai, H.-T.; Kim, S.-E. A simple higher-order shear deformation theory for bending and free vibration analysis of functionally graded plates. *Compos. Struct.* **2013**, *96*, 165–173, doi:10.1016/j.compstruct.2012.08.025.
36. Thai, H.-T.; Choi, D.-H. A simple first-order shear deformation theory for laminated composite plates. *Compos. Struct.* **2013**, *106*, 754–763, doi:10.1016/j.compstruct.2013.06.013.
37. Yin, S.; Hale, J.S.; Yu, T.; Bui, T.Q.; Bordas, S.P. Isogeometric locking-free plate element: A simple first order shear deformation theory for functionally graded plates. *Compos. Struct.* **2014**, *118*, 121–138, doi:10.1016/j.compstruct.2014.07.028.
38. Yu, T.T.; Yin, S.; Bui, T.Q.; Hirose, S. A simple FSDT-based isogeometric analysis for geometrically nonlinear analysis of functionally graded plates. *Finite Elem. Anal. Des.* **2015**, *96*, 1–10, doi:10.1016/j.finel.2014.11.003.
39. Zhang, D.-G.; Zhou, H.-M. Nonlinear bending analysis of FGM circular plates based on physical neutral surface and higher-order shear deformation theory. *Aerosp. Sci. Technol.* **2015**, *41*, 90–98, doi:10.1016/j.ast.2014.12.016.
40. Wang, C.; Koh, J.M.; Yu, T.; Xie, N.-G.; Cheong, K.H. Material and shape optimization of bi-directional functionally graded plates by GIGA and an improved multi-objective particle swarm optimization algorithm. *Comput. Methods Appl. Mech. Eng.* **2020**, *366*, 113017, doi:10.1016/j.cma.2020.113017.
41. Wang, S. A finite element model for the static and dynamic analysis of a piezoelectric bimorph. *Int. J. Solids Struct.* **2004**, *41*, 4075–4096, doi:10.1016/j.ijsolstr.2004.02.058.
42. Chowdhury, I.; Dasgupta, S.P. Computation of Rayleigh damping coefficients for large systems. *Electron. J. Geotech. Eng.* **2013**, *8*, 1–11, doi:10.0000/PMID509.
43. Liu, G.R.; Dai, K.Y.; Lim, K.M. Static and vibration control of composite laminates integrated with piezoelectric sensors and actuators using the radial point interpolation method. *Smart Mater. Struct.* **2004**, *13*, 1438–1447, doi:10.1088/0964-1726/13/6/015.
44. Tran, L.V.; Ferreira, A.; Nguyen-Xuan, H. Isogeometric analysis of functionally graded plates using higher-order shear deformation theory. *Compos. Part B Eng.* **2013**, *51*, 368–383, doi:10.1016/j.compositesb.2013.02.045.
45. Farsangi, M.A.A.; Saidi, A.R. Levy type solution for free vibration analysis of functionally graded rectangular plates with piezoelectric layers. *Smart Mater. Struct.* **2012**, *21*, 94017, doi:10.1088/0964-1726/21/9/094017.
46. Nguyen, N.V.; Nguyen, H.X.; Lee, S.; Nguyen-Xuan, H. Geometrically nonlinear polygonal finite element analysis of functionally graded porous plates. *Adv. Eng. Softw.* **2018**, *126*, 110–126, doi:10.1016/j.advengsoft.2018.11.005.
47. Wang, S.; Quek, S.; Ang, K. Dynamic stability analysis of finite element modeling of piezoelectric composite plates. *Int. J. Solids Struct.* **2004**, *41*, 745–764, doi:10.1016/j.ijsolstr.2003.09.041.

Publisher’s Note: MDPI stays neutral with regard to jurisdictional claims in published maps and institutional affiliations.



© 2020 by the authors. Licensee MDPI, Basel, Switzerland. This article is an open access article distributed under the terms and conditions of the Creative Commons Attribution (CC BY) license (<http://creativecommons.org/licenses/by/4.0/>).